Check for updates

ADVANCED ENERGY MATERIALS
www.advenergymat.de

Hybrid Molecular Photoanodes for Water Oxidation Based on Electropolymerized Cu Macrocyclic Complexes on $BiVO_4$-WO_3

Carlos G. Bellido, Michele Mazzanti, Koushik Ranu, Alberto Piccioni, Raffaello Mazzaro, Federico Boscherini, Fernando F. Salomón, Sergi Grau, Xavier Sala, Luca Pasquini,* Antoni Llobet,* and Stefano Caramori*

The conversion of sunlight into chemical energy provides a sustainable alternative to fossil fuels that can significantly contribute to the mitigation of climate change. In this regard, water splitting with sunlight using semiconductors coupled with redox catalysts emerges as a potential pathway to generate green hydrogen. Here, the performance of molecular hybrid materials composed of inorganic semiconductors, WO_3-$BiVO_4$, combined with molecular water oxidation catalysts based on Cu macrocyclic complexes is described. It is found that the charge transfer from $BiVO_4$ to the molecular catalyst occurs on a similar time scale to the direct interfacial hole transfer to water, with a concomitant 62% decrease in the recombination rate because recombination centers are passivated upon deposition of the Cu molecular catalyst on the WO_3-$BiVO_4$ junction. Overall, this results in an improvement of the photocurrent as well as long-term stability of the new hybrid materials generated.

1. Introduction

Solar fuels represent a promising strategy[1,2,3] for sustainable energy generation, offering a means to capture and utilize solar energy in a storable and usable form, such as hydrogen, that can contribute to the mitigation of climate change and enhance energy security. Photoelectrochemical cells (PECs), which employ light-absorbing materials and catalysts to drive electrochemical reactions, thereby enabling the efficient conversion of solar energy into chemical fuels such as hydrogen, are a promising avenue.[4,5] Hydrogen is a highly attractive energy vector due to its high gravimetric energy density (141.9 MJ kg^{-1}), which exceeds that of conventional fossil fuels (e.g., 46.4 MJ kg^{-1} for gasoline). Its conversion into electricity via fuel cells further enhances its appeal as a clean and efficient energy carrier for stationary, portable, and transportation applications. Currently, the vast majority of industrial hydrogen is produced from fossil fuels. Replacing this with green hydrogen derived from renewable energy sources could significantly reduce greenhouse gas emissions. Green hydrogen also offers medium- to large-scale and long-term energy storage capabilities, mitigates renewable energy curtailment, and supports the decarbonization of industry and transport through sector coupling strategies.

Metal oxide semiconductors are interesting materials for PEC devices due to their favorable stability, cost-effectiveness, nontoxicity, and light-harvesting properties across the visible spectrum. They are often employed as photoanodes in a tandem PEC configuration due to their deep valence band and relative

C. G. Bellido, K. Ranu, F. F. Salomón, S. Grau, A. Llobet
Institute of Chemical Research of Catalonia
Barcelona Institute of Science and Technology
Avda. Països Catalans, 16, Tarragona 43007, Spain
E-mail: allobet@iciq.cat

The ORCID identification number(s) for the author(s) of this article can be found under https://doi.org/10.1002/aenm.202500253

[+]Present address: Consiglio Nazionale delle Ricerche (CNR), Istituto Officina dei Materiali (IOM), c/o AREA Science Park, Trieste 34149, Italy

© 2025 The Author(s). Advanced Energy Materials published by Wiley-VCH GmbH. This is an open access article under the terms of the Creative Commons Attribution License, which permits use, distribution and reproduction in any medium, provided the original work is properly cited.

DOI: 10.1002/aenm.202500253

M. Mazzanti, S. Caramori
Department of Chemical
Pharmaceutical and Agricultural Sciences
University of Ferrara
Via Fossato di Mortara 17, Ferrara 44121, Italy
E-mail: mzzmhl3@unife.it

A. Piccioni, R. Mazzaro, F. Boscherini[+], L. Pasquini
Department of Physics and Astronomy "Augusto Righi"
Alma Mater Studiorum Università di Bologna
viale Berti-Pichat 6/2, Bologna 40127, Italy
E-mail: luca.pasquini@unibo.it

X. Sala
Departament de Química
Universitat Autònoma de Barcelona
Cerdanyola del Vallès, Barcelona 08193, Spain

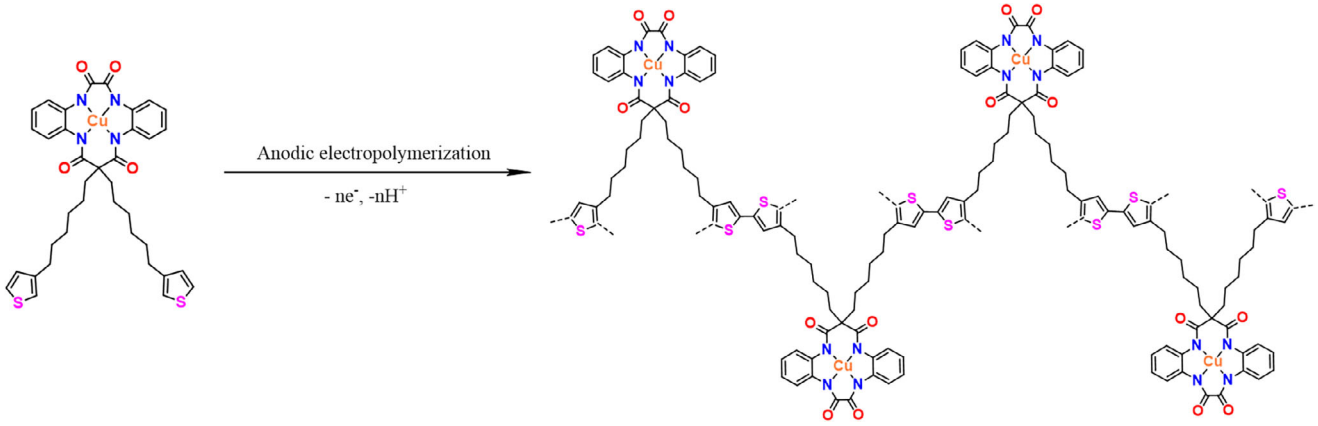

Figure 1. Anodic electropolymerization of the **[LCu]$^{2-}$** molecular catalyst monomer to generate a functionalized polythiophene thin film.

resistance against photocorrosion in oxidative environments, which enables them to drive the challenging oxygen evolution reaction (OER). For a successful device construction, these materials must efficiently absorb light, exhibit good bulk transport properties to separate the photogenerated charges, and induce rapid charge transfer from the electrode to the solution or to a catalyst to promote the OER. WO_3 and $BiVO_4$ are potential candidates as photoanodes for the water oxidation reaction.[6–10] $BiVO_4$ is a semiconductor that can be prepared in a nano-structured form with noteworthy spectral absorption characteristics (E_{gap} ≈2.5 eV) and values of the valence and conduction bands that are suitable for solar hydrogen generation from water. However, the low mobility of the charge carriers and the low stability of $BiVO_4$ under polarization and illumination preclude its effective use as a single junction. The formation of n-n junctions with porous materials such as WO_3 represents an interesting approach to address the issue of poor mobility of $BiVO_4$ carriers. However, efficient charge separation in the n-n junction still necessitates an additional positive potential to counteract carrier recombination. A common strategy to reduce the need for such a high positive potential is the utilization of a water oxidation catalyst (WOC) deposited on the surface of the light absorbing material to act as a hole transfer medium and thereby contributing to the decoupling of electrons and holes and to the photoelectrochemical stabilization of the photoanode against photocorrosion.

Most of the WOCs deposited on semiconductors described up to know are based on oxide materials,[11–14] while those based on molecules that retain their nature after the photocatalytic process are very scarce.[15] This is surprising since the molecular complexes can provide, via ligand design, a very fine tuning of the catalyst properties, both from a thermodynamic and kinetic perspective, and thus accommodate the demands dictated by the semiconductor.[16] A successful example that combines a *n*-Si semiconductor and a robust and efficient molecular Ru WOC has been described recently.[15] However, there are no examples of robust molecular WOCs based on first-row transition metals anchored on semiconductors where the integrity of the molecular species is unambiguously proven, for instance by X-ray absorption spectroscopy (XAS), in particular at pH 7. This is mainly due to the intrinsic lability of these complexes toward ligand substitution in aqueous solutions, that upon an applied potential, end up transforming themselves into the corresponding oxide materials.[17]

We have recently reported a family of Cu complexes containing tetraamidomacrocyclic ligands that, thanks to their macrocyclic and anionic nature, generate very strong Cu—N bonds and thus behave as very robust and efficient WOC even at neutral pH in homogeneous phase.[18,19] Among them we have shown that the **[LCu]$^{2-}$** (L is 15,15-bis(6-(thiophen-3-yl)hexyl)-8,13-dihydro-5H-dibenzo[b,h][1,4,7,10]tetraazacyclotridecine-6,7,14,16(15H,17H)-tetraone; See **Figure 1** for a drawing) complex can be anchored on graphitic surfaces and carry out efficient heterogeneous water oxidation electrocatalysis. We now like to turn our attention to anchoring molecular WOCs, but into inorganic semiconductors to explore their capacity to carry out light-induced water oxidation and to understand the interfacial interactions between the molecular catalysts and the light absorbing material.

Here we report on the electropolymerization of **[LCu]$^{2-}$** on $BiVO_4$-WO_3 n-n semiconductor heterojunctions to generate new hybrid materials, ***p*-[LCu]$^{2-}$@BiVO$_4$-WO$_3$**, that behave as robust and efficient light-induced WOCs.

2. Results and Discussion

2.1. Preparation, Characterization, and Photocatalytic Activity of Hybrid *p*-[LCu]$^{2-}$@BiVO$_4$-WO$_3$- Materials

Macrocyclic tetraamidate Cu(II) complexes are among the most robust molecular catalysts that carry out the oxidation of water to dioxygen efficiently at neutral pH.[18] We have recently described the functionalization of this type of catalyst using an alkyl thiophene unit at the propionic site of the ligand backbone, to generate a complex labeled as **[LCu]$^{2-}$**, whose structure is drawn in Figure 1. Under a sufficiently high anodic potential, the **[LCu]$^{2-}$** complex undergoes a thiophene electropolymerization, generating an insoluble film, labeled as ***p*-[LCu]$^{2-}$**, that firmly attaches to the surface of a graphitic electrode, as indicated in Figure 1.[20]

We now report the light-induced electropolymerization of complex **[LCu]$^{2-}$** on top of a **BiVO$_4$-WO$_3$** material generating ***p*-[LCu]$^{2-}$@BiVO$_4$-WO$_3$**, which acts as a hybrid semiconductor/molecular photoanode. This electropolymerization was achieved via chronoamperometry (CA) at E_{app} = 0.75 V versus

© 2025 The Author(s). Advanced Energy Materials published by Wiley-VCH GmbH

16146840, 2025, 40, Downloaded from https://advanced.onlinelibrary.wiley.com/doi/10.1002/aenm.202500253 by Area Sistemi Dipart & Doc, Wiley Online Library on [29/10/2025]. See the Terms and Conditions (https://onlinelibrary.wiley.com/terms-and-conditions) on Wiley Online Library for rules of use; OA articles are governed by the applicable Creative Commons License

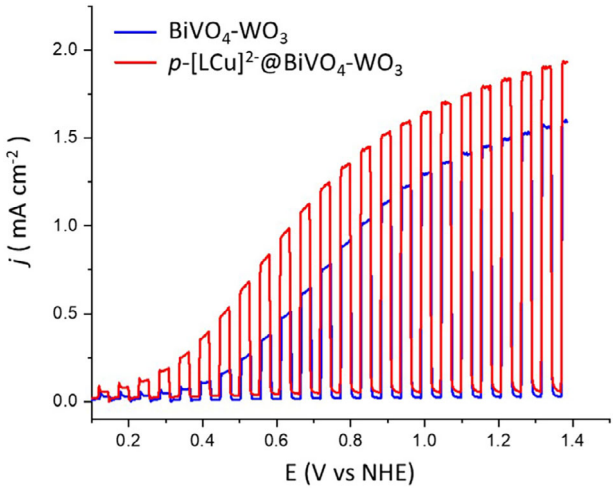

Figure 2. Chopped LSV under 1 sun irradiation (AM1.5G) of **$BiVO_4$-WO_3** (blue trace) and ***p*-[LCu]$^{2-}$@$BiVO_4$-WO_3** (red trace) electrodes in a 0.1 M phosphate buffer, pH 7 solution at a scan rate of 25 mV s^{-1}.

Fc^+/Fc for 5 min in a 3 mM **[LCu]**$^{2-}$ MeCN solution containing 0.1 M NH_4TfO as supporting electrolyte, under 1 sun illumination that gave the best results after trying several options (see Figures S3 and S4, Supporting Information). This generates the molecular hybrid material ***p*-[LCu]$^{2-}$@$BiVO_4$-WO_3** that was characterized by spectroscopy and microscopy techniques, including field emission scanning electron microscopy (FESEM) with energy dispersive X-ray spectroscopy (EDX), and XAS (Figures S13 and S14, Supporting Information). The amount of Cu deposited in this way was measured by inductively coupled plasma optical emission spectroscopy and turned out to be 37 nmol cm^{-2}.

The photoelectrochemical performance of the new material ***p*-[LCu]$^{2-}$@$BiVO_4$-WO_3** was analyzed by chopped light linear sweep voltammetry (LSV) under 1 sun illumination in a pH 7 phosphate buffer solution as shown in **Figure 2** (red trace) and compared to that of bare $BiVO_4$-WO_3 electrodes (Figure 2, blue trace) under the same conditions. The presence of the molecular catalyst enhances the photocurrent obtained within the potential range 0.0–1.4 V. The photocurrent enhancement is ≈20% (from 1.6 to 2.0 mA cm^{-2}) at E_{app} = 1.23 V, whereas at lower potential E_{app} = 0.70 V the enhancement is more than threefold (from 0.15 to 0.50 mA cm^{-2}). These data suggest that in the modified electrodes, a larger population of photogenerated holes escapes recombination and reaches the interface, where they react with the molecular Cu catalysts for the oxidation of water to dioxygen.

Incident photon to current efficiency (IPCE) spectra (**Figure 3**) show a 45% efficiency in the presence of the catalyst, which is similar to that recorded in the presence of a fast interfacial hole scavenger like SO_3^{2-}, suggesting that the holes that reach the interface with the electrolyte are not prone to recombination and are transferred with quantitative efficiency. Losses are thus mainly due to charge transport across the junction, and, based on the IPCE, they can be quantified as ≈50% of the initially generated electron/hole pairs. Indeed, since IPCE is expressed according to

$$IPCE = \phi_{e/h} \times \eta_{transport} \times \eta_{interface} \times LHE \quad (1)$$

where $\phi_{e/h}$ is the electron/hole generation quantum yield (unitary for a semiconductor) and *LHE* is the light harvesting efficiency (≈1 at λ<450 nm for this type of electrodes), $\eta_{interface}$ is the semiconductor/electrolyte interfacial charge transfer efficiency (assumed to be unitary in the presence of a fast hole scavenger like SO_3^{2-}) and $\eta_{transport}$ is the charge separation efficiency across the n/n junction formed by WO_3/$BiVO_4$, we can conclude that $\eta_{transport} \approx 50\%$ and that the presence of the electropolymerized molecular catalyst, ***p*-[LCu]$^{2-}$**, improves the charge separation across the semiconductor/electrolyte junction, which results from improvements in the product $\eta_{interface} \times \eta_{transport}$. At the microscopic level, the enhancement of the charge collection factor occurs either by boosting electron–hole separation at the $BiVO_4$/WO_3 interface or by passivation of recombination processes due to surface states or deep intra-bandgap trap states in the bulk. The investigation of the photohole lifetime by time-resolved spectroscopy will help to at least partially disentangle these effects (vide infra).

We note that SO_3^{2-} was used, instead of formate or methanol, to avoid the photocurrent doubling mechanisms by organic radicals, which would otherwise introduce an additional perturbation to a reliable estimation of the charge collection efficiency. For the bare photoanode without a molecular catalyst, the IPCE is lower, 40%, in line with the lower limiting photocurrent achieved. The absence of the molecular catalyst results in a larger portion of the photogenerated electrons (≈60%) recombining before being collected. Even the application of a high anodic potential, up to 1.4 V versus NHE, is not sufficient to suppress such recombination losses. This indicates that even in the presence of an ideal interfacial reaction, a sizable amount of charge is lost by recombination and that the charge transport efficiency is the likely limiting factor in determining the maximum photon-to-electron conversion yield in these photoanodes.

Consistent with the better results obtained in the presence of ***p*-[LCu]$^{2-}$** the maximum applied bias photocurrent efficiency (ABPE) of 0.60% is obtained for ***p*-[LCu]$^{2-}$@$BiVO_4$-WO_3** at 0.65 V

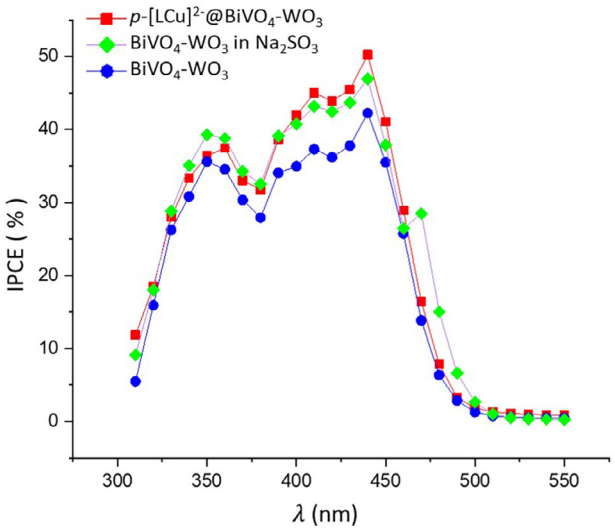

Figure 3. IPCE spectra at 1.15 V versus NHE of bare **$BiVO_4$-WO_3** (blue), ***p*-[LCu]$^{2-}$@$BiVO_4$-WO_3** (red) in a pH 7 μ = 0.1 M phosphate buffer solution, and **$BiVO_4$-WO_3** in the presence of a 0.5 M Na_2SO_3 (green).

© 2025 The Author(s). Advanced Energy Materials published by Wiley-VCH GmbH

16146840, 2025, 40, Downloaded from https://advanced.onlinelibrary.wiley.com/doi/10.1002/aenm.202500253 by Area Sistemi Dipart & Doc, Wiley Online Library on [29/10/2025]. See the Terms and Conditions (https://onlinelibrary.wiley.com/terms-and-conditions) on Wiley Online Library for rules of use; OA articles are governed by the applicable Creative Commons License

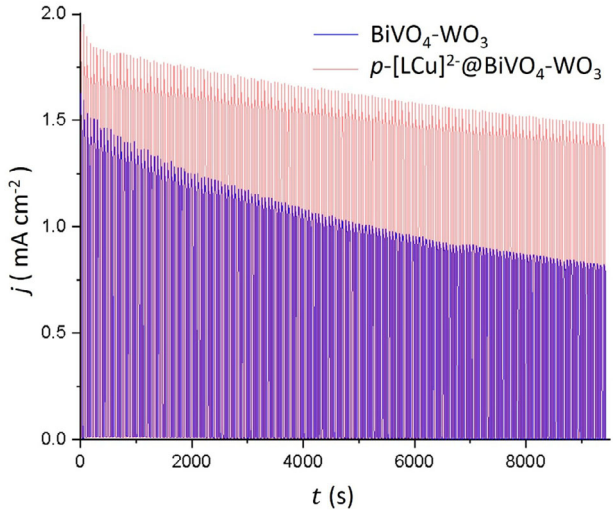

Figure 4. Chopped bulk electrolysis under 1 sun irradiation (AM1.5G) at 1.1 V versus NHE during 2.5 h in phosphate buffer 0.1 M, pH 7 of **$BiVO_4$-WO_3** (blue trace) and ***p*-[LCu]$^{2-}$@$BiVO_4$-WO_3** (red trace). The integrated currents result in total charges of 5.6 C (58.1 μmols of e^-) for **$BiVO_4$-WO_3** and 7.12 C (73.7 μmols of e^-) for ***p*-[LCu]$^{2-}$@$BiVO_4$-WO_3** that account for an overall TON of 1805, assuming 92% FE.

versus NHE which substantially doubles the ABPE observed in the absence of the catalysts (0.30%, at E_{app} = 0.78 V vs NHE) (Figure S5, Supporting Information). The higher ABPE value, observed at a lower bias in the presence of the ***p*-[LCu]$^{2-}$** arises from anticipated photocurrent onset and higher limiting current achieved with the latter. Both features are consistent with an improved electronic conductivity of WO_3/$BiVO_4$ junction as a consequence of reduced charge recombination.

To explore the long-term stability of the new molecular hybrid material ***p*-[LCu]$^{2-}$@$BiVO_4$-WO_3**, a chopped light bulk photoelectrolysis was carried out under 1 sun in a pH 7 phosphate buffer solution, for an interval of 2.5 h at E_{app} = 1.1 V versus NHE (1.51 vs RHE). The results in **Figure 4** show that the current density for ***p*-[LCu]$^{2-}$@$BiVO_4$-WO_3** drops by ≈12% at the end of the photoelectrolysis, much less than in the unmodified **$BiVO_4$-WO_3** electrode (36% drop), highlighting the increased stability of the photoanode in the presence of the molecular layer. Overall, 5.6 C (58.1 mmols of e^-) and 7.12 C (73.7 mmols of e^-) were passed for **$BiVO_4$-WO_3** and ***p*-[LCu]$^{2-}$@$BiVO_4$-WO_3** respectively, showing again the higher activity of the semiconductor functionalized by the molecular catalyst. Faradaic efficiencies (FEs) were calculated using a Clark electrode placed within the space head of the working compartment and running a constant potential electrolysis (CPE) under the same conditions as above and at E_{app} = 1.3 V versus NHE for 1 h (see Figure S7, Supporting Information). For the unmodified **$BiVO_4$-WO_3** electrode and for ***p*-[LCu]$^{2-}$@$BiVO_4$-WO_3**, FEs of 70 and 92% were obtained, respectively. With these values, a turnover number (TON) of 1.8×10^3 is determined for the Cu molecular catalysts.

The increased photoanodic stability in the presence of the electropolymerized molecular catalyst, ***p*-[LCu]$^{2-}$**, together with the sharp increase in Faradaic efficiency, clearly indicates that the molecular catalyst has an active role in the interfacial electron transfer, and, besides reducing recombination, decreases the irreversible parasitic corrosion of the **$BiVO_4$-WO_3** semiconductor upon illumination.[21–24] This suggests that the known instability of $BiVO_4$ could be mitigated by exploiting other types of catalytic overlayers incorporating metal oxide catalysts or metallopolymeric species.[25,26]

The photoanodes were further characterized by X-ray absorption near-edge structure (XANES) and extended X-ray absorption fine structure (EXAFS) at Cu K-edge, to probe the oxidation state and the local environment of the metal center. **Figure 5a** reports the XANES spectra for ***p*-[LCu]$^{2-}$@$BiVO_4$-WO_3** before and after the photoelectrolysis experiment, as well as the ones for pristine **[LCu]$^{2-}$** and CuO, used as reference samples. A slight variation of the XANES spectrum for ***p*-[LCu]$^{2-}$@$BiVO_4$-WO_3** is observed, with respect to pristine **[LCu]$^{2-}$**. Similarly, EXAFS analysis (Figure 5b; Supporting Information) reveals a small expansion of the first coordination sphere, signaled by the increased average Cu-N distance from 1.88 Å for the **[LCu]$^{2-}$** powder to 1.93 Å for the Cu complex ***p*-[LCu]$^{2-}$** electropolymerized on the surface of **$BiVO_4$-WO_3**. This expansion, albeit limited, indicates a distortion of the complex basal plane due to an interaction with the semiconductor surface. More importantly, both XANES and EXAFS confirm that ***p*-[LCu]$^{2-}$@$BiVO_4$-WO_3** structure is not affected by the photoelectrolysis, pointing out the robustness of the molecular catalysts. Finally, XAS demonstrates that the formation of CuO with consequent irreversible degradation of the molecular catalysts does not occur. This is particularly evident in the XANES spectra of ***p*-[LCu]$^{2-}$@$BiVO_4$-WO_3**, which strongly differ from that of reference, crystalline CuO, both before and after the photoelectrolysis (Figure 5a). Even the quantitative analysis of EXAFS spectra confirms the difference between the local structure of ***p*-[LCu]$^{2-}$@$BiVO_4$-WO_3** and CuO (see EXAFS fit parameters reported in Tables S2 and S3, Supporting Information). Additional evidence in favor of the stability of ***p*-[LCu]$^{2-}$@$BiVO_4$-WO_3** is provided by resonance Raman spectroscopy experiments (see Figure S17, Supporting Information), where CuO is not detected. Along with the bulk electrolysis described above (Figure 4), this indicates that the progressive loss of activity (12% after 2.5 h) is most likely associated with the de-anchoring of the catalyst from the electrode surface, rather than deactivation paths generating CuO. This conclusion is corroborated by the comparison between non-normalized XANES spectra before and after photoelectrolysis shown in Figure S16 (Supporting Information): the lower jump observed at the K-edge after photoelectrolysis indicates a lower density of Cu atoms at the surface, consistent with a partial loss of catalyst due to de-anchoring.

2.2. Interfacial Electron Transfer Kinetics and Mechanistic Insights from Transient Absorption Spectroscopy

The transient absorption spectrum (TAS) of **$BiVO_4$-WO_3** in a pH 7 μ = 0.1 M phosphate buffer solution at the ms timescale range is reported in **Figure 6a**. Consistent with previous reports from Kamat[27] a 470 nm absorption peak, assigned to trapped holes in $BiVO_4$, is followed by a weaker structureless absorption extending into the NIR, also assigned to hole absorption in $BiVO_4$. A modulation of the intensity due to interference fringes originated by the multilayered photoanode architecture is also evident ≈650 nm.

© 2025 The Author(s). Advanced Energy Materials published by Wiley-VCH GmbH

16146840, 2025, 40, Downloaded from https://advanced.onlinelibrary.wiley.com/doi/10.1002/aenm.202500253 by Area Sistemi Dipart & Doc, Wiley Online Library on [29/10/2025]. See the Terms and Conditions (https://onlinelibrary.wiley.com/terms-and-conditions) on Wiley Online Library for rules of use; OA articles are governed by the applicable Creative Commons License

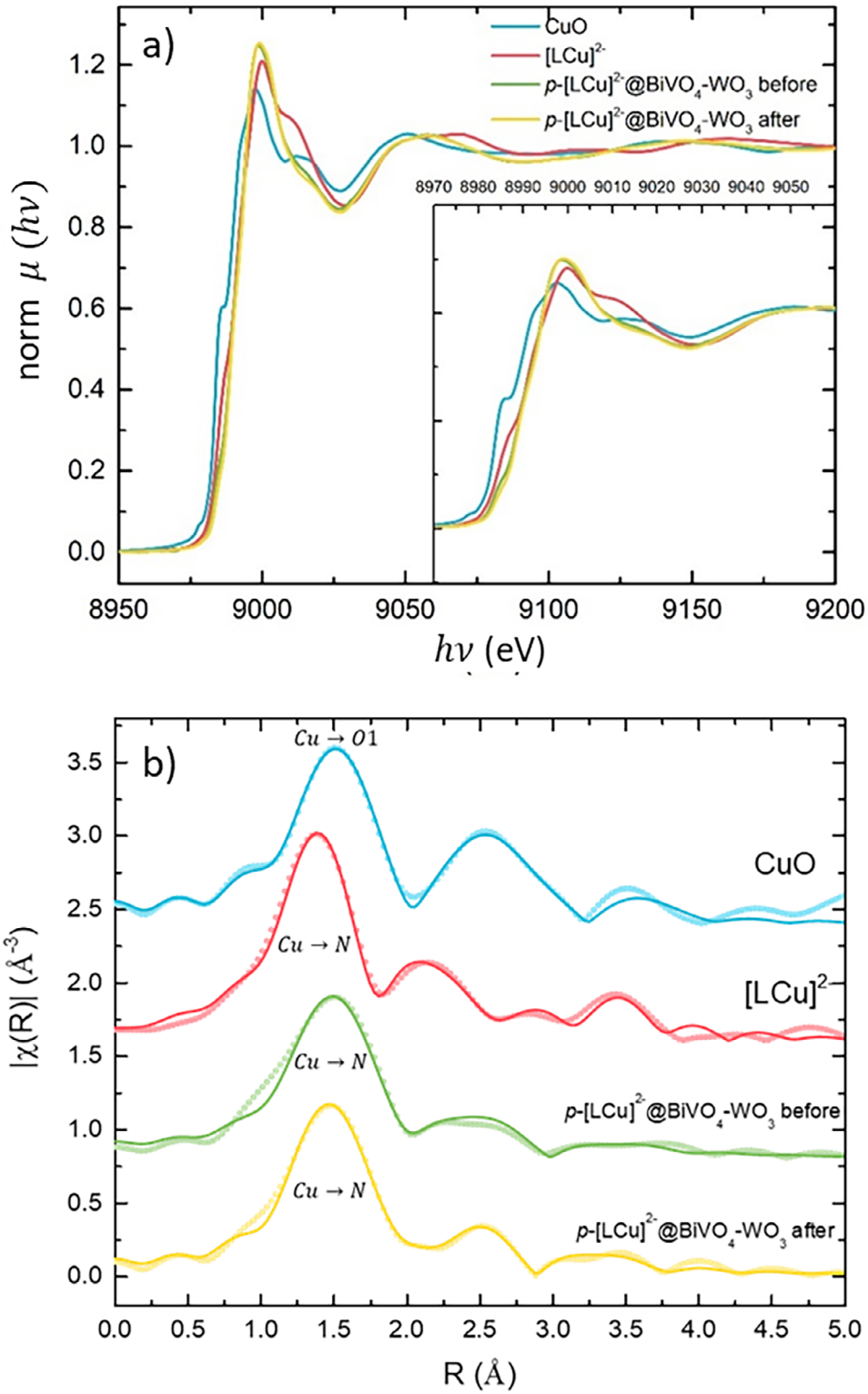

Figure 5. a) normalized Cu K-edge XANES of **[LCu]$^{2-}$** powder (red trace), **CuO** powder (blue trace), and ***p*-[LCu]$^{2-}$@BiVO$_4$-WO$_3$** before (green trace) and after catalysis for over 400 TONs (yellow trace). The inset shows an enlargement of the XANES in the 8970–9060 eV region. b) experimental Fourier transforms of k^2-weighted EXAFS spectra (dotted lines) and fittings (solid lines). See dedicated paragraphs and Figure S15 (Supporting Information) for additional experimental details and quantitative analysis.

© 2025 The Author(s). Advanced Energy Materials published by Wiley-VCH GmbH

16146840, 2025, 40, Downloaded from https://advanced.onlinelibrary.wiley.com/doi/10.1002/aenm.202502253 by Area Sistemi Dipart & Doc, Wiley Online Library on [29/10/2025]. See the Terms and Conditions (https://onlinelibrary.wiley.com/terms-and-conditions) on Wiley Online Library for rules of use; OA articles are governed by the applicable Creative Commons License

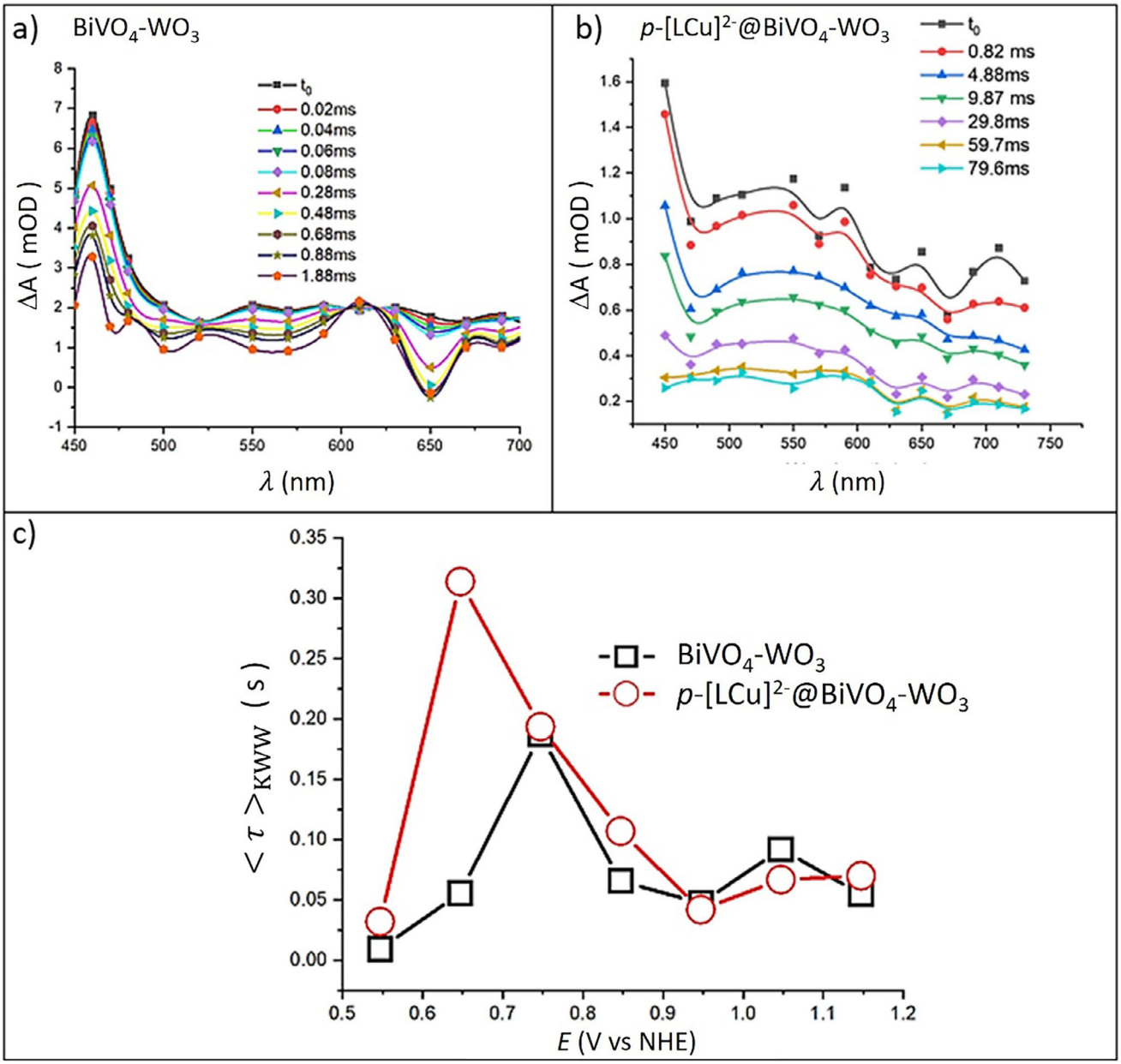

Figure 6. Transient absorption spectra at different time delays following 355 nm laser excitation in a $\mu = 0.1$ M phosphate buffer at pH 7 of a) **$BiVO_4$-WO_3** and b) ***p*-$[LCu]^{2-}$@$BiVO_4$-WO_3** (open circuit conditions). c) Average lifetime (in seconds) of transient absorption at 500 nm as a function of the applied voltage computed from KWW fitting of the kinetic data reported in Figure S8 (Supporting Information).

Similar features are observed in the TAS of ***p*-$[LCu]^{2-}$@$BiVO_4$-WO_3** reported in Figure 6b, showing that the contribution of ***p*-$[LCu]^{2-}$** to the transient absorption is negligible. Thus, TAS allows to track the time evolution of photoholes generated and residing inside $BiVO_4$, but the spectroscopic signature of the oxidized catalyst cannot be directly observed with this technique. Referring to Figure 6b, recorded at open circuit potential, we observe a stronger 500–700 nm absorption compared to the sharp absorption feature centered ≈460–470 nm. The intensity of the hole absorption in the ***p*-$[LCu]^{2-}$** sensitized film is also generally larger than that reported in Figure 6a, suggesting the persistence of longer-lived carriers in the ***p*-$[LCu]^{2-}$** modified electrode. The 500 nm absorption is generally long-lived, extending well into the 0.1 s time scale, and its amplitude is increased under positive bias (Figure S8, Supporting Information), corroborating our assignment to the spectroscopic signature of photoholes. Indeed, the enhanced ΔA under positive potential is consistent with improved spatial electron/hole separation. Such a process is driven by an electrochemical potential gradient between the regions where carriers are generated and the interfaces where carriers are consumed. Specifically, in this type of n-n junction, holes are injected into the electrolyte, and electrons are drawn into the fluorine-doped tin oxide (FTO) collector via WO_3, which acts as an electron transporting medium.

© 2025 The Author(s). Advanced Energy Materials published by Wiley-VCH GmbH

16146840, 2025, 40, Downloaded from https://advanced.onlinelibrary.wiley.com/doi/10.1002/aenm.202500253 by Area Sistemi Dipart & Doc, Wiley Online Library on [29/10/2025]. See the Terms and Conditions (https://onlinelibrary.wiley.com/terms-and-conditions) on Wiley Online Library for rules of use; OA articles are governed by the applicable Creative Commons License

The 500 nm decays (Figure S8, Supporting Information) could be well fitted with Kohlrausch-Williams-Watts (KWW) functions, accounting for a distribution of rate constants originated by the inherently inhomogeneous nature of these nanostructured electrodes.[28]

In ***p*-[LCu]$^{2-}$@BiVO$_4$-WO$_3$** the normalized transient photohole amplitudes reproduce well the *j–V* behavior of the photoelectrodes measured in the same optical setup used for TAS measurements (Figure S9a, Supporting Information), confirming that the 500 nm transient signal is physically related to the photocurrent generation mechanism in the n/n junction. We also observe that although the amplitudes at the 0.64–1.15 V versus NHE interval are in remarkable agreement with the current/voltage characteristic, the 500 nm amplitude taken at 0.54 V lies outside the trend dictated by the *j–V* curve. This suggests that photoholes generated at this voltage, where the electrochemical potential gradient is not yet effective in promoting photocurrent generation, undergo mostly slow recombination via surface states and do not contribute to the photocurrent.

The correlation of the photohole amplitude with the *j–V* curve is found also with the unmodified **BiVO$_4$-WO$_3$** photoanode (Figure S9b, Supporting Information), but in this case the correlation is less satisfactory mostly due to the instability of the bare electrode, not protected by ***p*-[LCu]$^{2-}$**, in phosphate buffer and subjected to cycles of UV excitation and polarization of several minutes. Similar to the previous case, the 0.54 V 500 nm amplitude lies outside of the curve but, in general, a larger scattering of the amplitudes is observed at each voltage for the reason mentioned above.

The voltage dependences of the average lifetime $\langle\tau\rangle$ determined from KWW fits (Figure 6c) in the two electrodes are similar. Initially, the lifetime increases with increasing voltage, indicating that recombination is slowed down by the increasing electrochemical potential gradient inside the semiconductor. A maximum is achieved in the 0.64–0.74 V versus NHE interval, which corresponds to the inflection point of each *j–V* curve where the semiconductor electrode exhibits its highest conductivity (Figure S10, Supporting Information). Indeed, a longer-lived density of charge carriers inside the semiconductor translates into improved conductivity of the photoanode. Both the lifetime and the conductivity of the ***p*-[LCu]$^{2-}$@BiVO$_4$-WO$_3$** are significantly higher than in the unmodified **BiVO$_4$-WO$_3$** at 0.64–0.74 V versus NHE. As the voltage increases past 0.84 V, the lifetime in both electrodes decreases, due to the sweeping of the holes at the interface where they are consumed. The photohole lifetime of both electrodes is substantially aligned (≈0.05–0.1 s) above 0.9 V versus NHE, suggesting that interfacial transfer of holes proceeds here at an analogous rate, irrespective of the presence of ***p*-[LCu]$^{2-}$** at the interface. We also note that, in neither case, even at the limiting current voltage, the IPCE was quantitative (Figure 3). Maximum values in the order of 50% were observed (Figure 3), indicating that bulk and surface recombination remained always competitive with interfacial charge transfer. The electrode photocorrosion, which is certainly active at least in the unmodified **BiVO$_4$-WO$_3$**, adds another undesired carrier scavenging pathway to this complicated picture. Thus, it was not possible to directly obtain a true interfacial charge transfer rate constant for the water oxidation reaction of interest. However, by considering that ≈0.65–0.7 V (the voltage range at which we observe the largest difference in lifetime and conductivity between ***p*-[LCu]$^{2-}$@BiVO$_4$-WO$_3$** and unmodified **BiVO$_4$-WO$_3$**) the photocurrent is about 50% of the limiting value (Figure S9, Supporting Information, curves taken during TAS experiments), we assume that the maximum IPCE at 450 nm scales accordingly by a factor 0.5 and is about 25% at 0.65–0.7 V. IPCE is controlled by the factor $k_{bulk}/(k_{bulk}+k_{rec})$ where k_{bulk} here represents an effective kinetic constant governing the charge separation in the bulk, which is comprehensive of charge transport (ultimately resulting in the injection in the charge collecting phases), bulk recombination, and parasitic photocorrosion (this one may actually occur both in the bulk and at the surface). Details of the calculations are provided in Equations (S8)–(S12) (Supporting Information). We remark that the terms "bulk" and "surface" should be considered with caution, because the nanostructured electrode is constituted by interconnected particles permeated by the electrolyte. Thus, it becomes difficult to truly separate bulk from interfacial processes, since a given carrier moving toward the respective collecting phase (FTO for electrons, electrolyte for holes) may traverse several interfaces before being measured as a photocurrent. k_{rec} is the "surface" recombination rate constant[29] and assuming that $<\tau> = 1/(k_{bulk}+k_{rec}) \approx 0.3$ s (Figure 6c) we obtain a k_{bulk} of 0.83 s^{-1} (Equation S8, Supporting Information), in good agreement with interfacial hole transfer rate constant values of ≈1 s^{-1} reported by Durrant and coworkers for bare BiVO$_4$.[30,31] Therefore, ***p*-[LCu]$^{2-}$** does not appear to boost interfacial charge transfer, suggesting that its beneficial role is that of a recombination passivating agent. Larger hole-related TAS amplitudes (which means larger photohole densities at comparable voltage compared to the unmodified electrode) associated to a longer photohole lifetime obtained in the presence of ***p*-[LCu]$^{2-}$** is the plausible cause of the enhanced photocurrent even in the absence of a substantial acceleration of the interfacial transfer kinetics from BiVO$_4$ to ***p*-[LCu]$^{2-}$** because it allows for the achievement of an increased density of useful carriers. Last, we were able to confirm longer recombination lifetimes and larger interfacial hole density in the presence of ***p*-[LCu]$^{2-}$** by observing the recombination transients at the onset of the *j–V* curves, by exploiting a shuttered illumination source (Figure S11, Supporting Information), which, together with the O_2 evolution measurements provides a further indication that the ***p*-[LCu]$^{2-}$** is participating to the interfacial hole transfer and not merely acting as a passivating agent. At the onset of each *j–V* curve, the electrochemical potential gradient is unable to achieve a quantitative separation of electron and holes, and a cathodic spike, observed upon shutting off the illumination is usually observed, originated by the recombination of electrons with holes trapped in surface states (which could well represent oxidized ***p*-[LCu]$^{2-}$** when the latter is present). Usually, these recombination kinetics are slow, and extend well into the 1 s time scale; thus, they partly exceed the timescale of the TAS experiments and may contribute to the residual hole amplitude often observed at low voltage in the TAS kinetics. We observe that when ***p*-[LCu]$^{2-}$** is present, the charge trapped in surface states is ca. twice that of bare BiVO$_4$ (Figure S12, Supporting Information). Such a ratio increases to a factor of 10 at 0.74 V, while back recombination occurs on a time scale of a few seconds (Figure S8, Supporting Information). In addition, by looking at the photocurrent transients of ***p*-[LCu]$^{2-}$@BiVO$_4$-WO$_3$** in Figure S11 (Supporting Information), we observe a progressive

© 2025 The Author(s). Advanced Energy Materials published by Wiley-VCH GmbH

16146840, 2025, 40, Downloaded from https://advanced.onlinelibrary.wiley.com/doi/10.1002/aenm.202500253 by Area Sistemi Dipart & Doc, Wiley Online Library on [29/10/2025]. See the Terms and Conditions (https://onlinelibrary.wiley.com/terms-and-conditions) on Wiley Online Library for rules of use; OA articles are governed by the applicable Creative Commons License

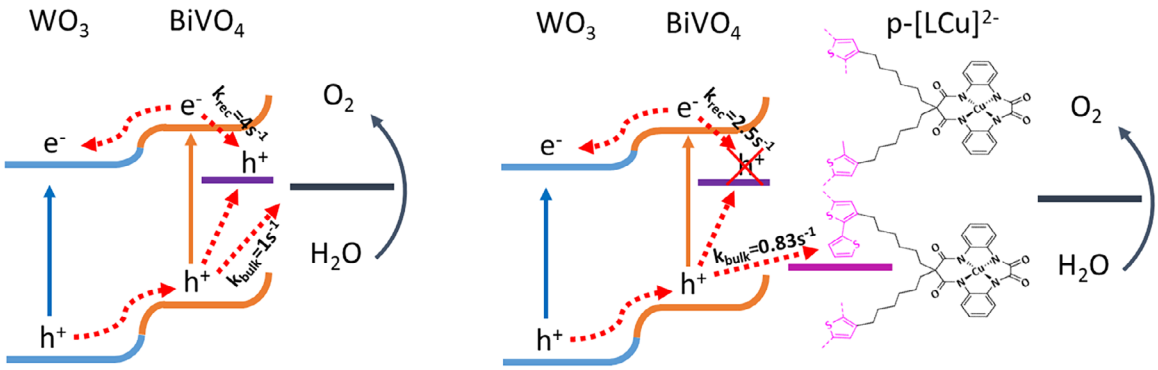

Scheme 1. Schematic representation of the charge transfer mechanism with and without ***p*-[LCu]$^{2-}$** correlated with the recombination and charge transfer rate constants estimated by combining TAS and photoelectrochemical measurements at a voltage of 0.65 V versus NHE.

increase of the cathodic surface recombination spikes, which is also indicative of hole accumulation in the electroactive **[LCu]$^{2-}$** surface layer upon subsequent illumination cycles. If we consider that the TAS kinetics at 0.74 V are essentially complete, meaning that holes have left $BiVO_4$ within a time scale of $3<\tau> \approx 0.5$ s (see Figure 6c), we can infer that such a large and slow recombination process involves holes trapped into ***p*-[LCu]$^{2-}$**. The decoupling between holes trapped in the ***p*-[LCu]$^{2-}$** layer and electrons left in $BiVO_4$ is thus consistent with both the larger photocharge and longer lifetime for the transient recombination involving surface states. These states are thus available for promoting water oxidation. Transfer of holes to the catalyst would also inhibit electrode photocorrosion, consistent with the more stable performance of ***p*-[LCu]$^{2-}$@BiVO$_4$-WO$_3$** under prolonged photoelectrolysis conditions.

3. Conclusion

Overall, we conclude that the charge transfer from $BiVO_4$ to the molecular catalyst occurs on a similar time scale to the direct interfacial hole transfer to water, with a concomitant 62% decrease in the recombination rate because recombination centers are passivated upon deposition of the Cu molecular catalyst on the $WO_3/BiVO_4$ junction. Based on the photoelectrochemical and spectroscopic investigation we propose in **Scheme 1**, that both water oxidation and hole transfer to the ***p*-[LCu]$^{2-}$** surface layer occur on a similar time scale of ≈ 1 s^{-1}, but in the absence of the molecular catalyst this time constant also incorporates the $BiVO_4$ corrosion, which we have shown to occur already on a time scale of a few tens of minutes. The photohole-induced corrosion also affects the apparent hole k_{rec} (4 s^{-1} Equation S13, Supporting Information), which is substantially reduced when ***p*-[LCu]$^{2-}$** is present (2.5 s^{-1} Equation S8, Supporting Information). These values are given at a voltage of 0.64 V versus NHE, which corresponds to the voltage range where the conductivity of these photoelectrodes reaches their respective maxima. The study of photoanodic transients, of electrode stability and the faradaic efficiency of oxygen evolution concur to indicate that ***p*-[LCu]$^{2-}$** is not a mere passivating agent in ***p*-[LCu]$^{2-}$@BiVO$_4$-WO$_3$** but that rather ***p*-[LCu]$^{2-}$** is actively involved in mediating the charge transfer reactions to the electrolyte, resulting in improved and more stable performance of ***p*-[LCu]$^{2-}$@BiVO$_4$-WO$_3$** under prolonged photoelectrolysis conditions.

Supporting Information

Supporting Information is available from the Wiley Online Library or from the author.

Acknowledgements

C.G.B., M.M., and K.R. contributed equally to this work. This project has received funding from the European Union's Horizon 2020 research and innovation programme, under Grant Agreement No 101006839 (H2020 Research Innovation Actions 2020–2024 "CONDOR"). KR acknowledges the award of a PhD grant from ICIQ. AL acknowledges CERCA Program/Generalitat de Catalunya and Severo Ochoa Excellence Accreditation CEX2024-001469-S funded by MCIU/AEI/10.13039/501100011033, MICINN through project PID2022-140143OB-I00 and Generalitat de Catalunya for the project 2021 SGR 01583. LP, RM, and FB acknowledge the European Synchrotron Radiation Facility (ESRF) and the CERIC-ERIC Consortium for the provision of beamtime under proposals number CH-6248 and A08-1-1118, and would like to thank the staff of beamline BM08 for their excellent support.

Open access publishing facilitated by Universita degli Studi di Bologna, as part of the Wiley - CRUI-CARE agreement.

Conflict of Interest

The authors declare no conflict of interest.

Data Availability Statement

The data that support the findings of this study are available from the corresponding author upon reasonable request.

Keywords

light absorbing materials, molecular hybrid materials, molecular water oxidation catalysts, solar fuels

Received: January 13, 2025
Revised: July 18, 2025
Published online: August 29, 2025

[1] J. H. Kim, D. Hansora, P. Sharma, J.-W. Jang, J. S. Lee, *Chem. Soc. Rev.* **2019**, *48*, 1908.

© 2025 The Author(s). Advanced Energy Materials published by Wiley-VCH GmbH

16146840, 2025, 40, Downloaded from https://advanced.onlinelibrary.wiley.com/doi/10.1002/aenm.202500253 by Area Sistemi Dipart & Doc, Wiley Online Library on [29/10/2025]. See the Terms and Conditions (https://onlinelibrary.wiley.com/terms-and-conditions) on Wiley Online Library for rules of use; OA articles are governed by the applicable Creative Commons License

[2] E. A. Schneider, M. R. Deinert, K. B. Cady, *Energy Econ.* **2009**, *31*, 627.
[3] K. Maeda, K. Domen, *J. Phys. Chem. Lett.* **2010**, *1*, 2655.
[4] C. Jiang, S. J. A. Moniz, A. Wang, T. Zhang, J. Tang, *Chem. Soc. Rev.* **2017**, *46*, 4645.
[5] M. G. Walter, E. L. Warren, J. R. McKone, S. W. Boettcher, Q. Mi, E. A. Santori, N. S. Lewis, *Chem. Rev.* **2010**, *110*, 6446.
[6] C. C. L. McCrory, S. Jung, I. M. Ferrer, S. M. Chatman, J. C. Peters, T. F. Jaramillo, *J. Am. Chem. Soc.* **2015**, *137*, 4347.
[7] Z.-F. Huang, L. Pan, J.-J. Zou, X. Zhang, L. Wang, *Nanoscale* **2014**, *6*, 14044.
[8] C. A. Bignozzi, S. Caramori, V. Cristino, R. Argazzi, L. Meda, A. Tacca, *Chem. Soc. Rev.* **2013**, *42*, 2228.
[9] F. S. Hegner, I. Herraiz-Cardona, D. Cardenas-Morcoso, N. López, J.-R. Galán-Mascarós, S. Gimenez, *ACS Appl. Mater. Interfaces* **2017**, *9*, 37671.
[10] Y. Park, K. J. McDonald, K.-S. Choi, *Chem. Soc. Rev.* **2013**, *42*, 2321.
[11] F. F. Abdi, L. Han, A. H. M. Smets, M. Zeman, B. Dam, R. van de Krol, *Nat. Commun.* **2013**, *4*, 2195.
[12] B. Moss, F. S. Hegner, S. Corby, S. Selim, L. Francàs, N. López, S. Giménez, J.-R. Galán-Mascarós, J. R. Durrant, *ACS Energy Lett.* **2019**, *4*, 337.
[13] C. Zachäus, F. F. Abdi, L. M. Peter, R. van de Krol, *Chem. Sci.* **2017**, *8*, 3712.
[14] P. Vecchi, A. Piccioni, R. Mazzaro, M. Mazzanti, V. Cristino, S. Caramori, L. Pasquini, *Sol. RRL* **2022**, *6*, 2200108.
[15] R. Matheu, I. A. Moreno-Hernandez, X. Sala, H. B. Gray, B. S. Brunschwig, A. Llobet, N. S. Lewis, *J. Am. Chem. Soc.* **2017**, *139*, 11345.
[16] B. Zhang, L. Sun, *Chem. Soc. Rev.* **2019**, *48*, 2216.
[17] P. Pelosin, M. Gil-Sepulcre, P. Garrido-Barros, D. Moonshiram, J. Benet-Buchholz, C. Gimbert-Suriñach, A. Llobet, *iScience* **2020**, *23*, 101378.
[18] P. Garrido-Barros, I. Funes-Ardoiz, S. Drouet, J. Benet-Buchholz, F. Maseras, A. Llobet, *J. Am. Chem. Soc.* **2015**, *137*, 6758.
[19] P. Garrido-Barros, C. Gimbert-Suriñach, D. Moonshiram, A. Picón, P. Monge, V. S. Batista, A. Llobet, *J. Am. Chem. Soc.* **2017**, *139*, 12907.
[20] S. Amthor, K. Ranu, C. G. Bellido, F. F. Salomón, A. Piccioni, R. Mazzaro, F. Boscherini, L. Pasquini, M. Gil-Sepulcre, A. Llobet, *Adv. Mater.* **2024**, *36*, 2308392.
[21] S. Zhang, M. Rohloff, O. Kasian, A. M. Mingers, K. J. J. Mayrhofer, A. Fischer, C. Scheu, S. Cherevko, *J. Phys. Chem. C* **2019**, *123*, 23410.
[22] M. Arunachalam, K. Lee, K. Zhu, S. H. Kang, *Adv. Energy Mater.* **2024**, *14*, 2402607.
[23] R. Gao, L. Wang, *Angew. Chem., Int. Ed.* **2020**, *59*, 23094.
[24] X. Yao, X. Zhao, J. Hu, H. Xie, D. Wang, X. Cao, Z. Zhang, Y. Huang, Z. Chen, T. Sritharan, *iScience* **2019**, *19*, 976.
[25] S. S. Kalanur, I.-H. Yoo, J. Park, H. Seo, *J. Mater. Chem. A Mater.* **2017**, *5*, 1455.
[26] X. Yao, D. Wang, X. Zhao, S. Ma, P. S. Bassi, G. Yang, W. Chen, Z. Chen, T. Sritharan, *Energy Technol.* **2018**, *6*, 100.
[27] I. Grigioni, K. G. Stamplecoskie, E. Selli, P. V. Kamat, *J. Phys. Chem. C* **2015**, *119*, 20792.
[28] M. S. Eberhart, D. Wang, R. N. Sampaio, S. L. Marquard, B. Shan, M. K. Brennaman, G. J. Meyer, C. Dares, T. J. Meyer, *J. Am. Chem. Soc.* **2017**, *139*, 16248.
[29] A. Reddy-Marri, E. Marchini, V. D. Cabanes, R. Argazzi, M. Pastore, S. Caramori, P. C. Gros, *Chem. Sci.* **2023**, *14*, 4288.
[30] S. Selim, L. Francàs, M. García-Tecedor, S. Corby, C. Blackman, S. Gimenez, J. R. Durrant, A. Kafizas, *Chem. Sci.* **2019**, *10*, 2643.
[31] Y. Ma, F. Le Formal, A. Kafizas, S. R. Pendlebury, J. R. Durrant, *J. Mater. Chem. A Mater.* **2015**, *3*, 20649.

© 2025 The Author(s). Advanced Energy Materials published by Wiley-VCH GmbH

16146840, 2025, 40, Downloaded from https://advanced.onlinelibrary.wiley.com/doi/10.1002/aenm.202500253 by Area Sistemi Dipart & Doc, Wiley Online Library on [29/10/2025]. See the Terms and Conditions (https://onlinelibrary.wiley.com/terms-and-conditions) on Wiley Online Library for rules of use; OA articles are governed by the applicable Creative Commons License